Article:

Segura, N.C., Pelisoli, I. orcid.org/0000-0003-4615-6556, Gänsicke, B.T. et al. (21 more authors) (2025) A sibling of AR Scorpii: SDSS J230641.47+244055.8 and the observational blueprint of white dwarf pulsars. Monthly Notices of the Royal Astronomical Society. staf1511. ISSN: 0035-8711

https://doi.org/10.1093/mnras/staf1511

A Sibling of AR Scorpii: SDSS J230641.47+244055.8 and the Observational Blueprint of White Dwarf Pulsars

N. Castro Segura 1★, I. Pelisoli 1, B. T. Gänsicke 1, D. L. Coppejans 1, D. Steeghs 1,
A. Aungwerojwit 2, K. Inight 1, A. Romero 3, A. Sahu 1, V. S. Dhillon 4,5, J. Munday 1,
S. G. Parsons 4, M. R. Kennedy 6, M. J. Green 7,8 A. J. Brown 9, M. J. Dyer 4, E. Pike4,
J. A. Garbutt4, D. Jarvis4, P. Kerry4, S. P. Littlefair 4, J. McCormac1, D. I. Sahman4,
D. A. H. Buckley 10,11

Affiliations are listed at the end of the paper

Accepted XXX. Received YYY; in original form ZZZ

ABSTRACT

Radio pulsating white dwarf (WD) systems, known as WD pulsars, are binary systems where the rapidly spinning WD interacts with a low-mass companion, producing pulsed non-thermal emission observed across the entire electromagnetic spectrum. Only two such systems are known: AR Sco and eRASSU J191213.9−441044. Here we present the discovery of a third WD pulsar, SDSS J230641.47+244055.8. The optical spectrum is dominated by molecular bands from an M-dwarf companion, with additional narrow Balmer and He I lines. The long-term optical light-curve folded on its orbital period ($P_{\rm orb}$ = 3.49 h) shows ∼ 10 per cent scatter. High-cadence photometry reveals a short period signal, which we interpret to be the spin period of the WD primary ($P_{\rm spin} \simeq 92$ s). The WD spin period is slightly shorter than that of AR Sco (∼ 117 s), the WD pulsar prototype. Time-resolved spectroscopy reveals emission from the irradiated companion and Na I absorption tracing its centre of mass, yielding a binary mass function of $f(M) \simeq 0.2\,{\rm M}_\odot$. The H$\alpha$ emission includes a low-amplitude broad component, resembling the energetic flashes seen in AR Sco. Using spectral templates, we classify the companion to be most likely a M4.0 ± 0.5 with $T_{\rm eff} \approx 3300$ K. Modelling the stellar contribution constrains the secondary mass ($0.19\,{\rm M}_\odot \lesssim M_2 \lesssim 0.28\,{\rm M}_\odot$), distance ($\simeq 1.2$ kpc), and inclination ($i \simeq 45 - 50°$). We discuss the proposed evolutionary scenarios and summarise the observational properties of all three known WD pulsars, establishing a benchmark for identifying and classifying future members of this class.

Key words: binaries: general – cataclysmic variables – binaries: close – stars: individual: SDSS J230641.47+244055.8

1 INTRODUCTION

White dwarf (WD) pulsars are binary systems composed of a nearly Roche lobe filling late-type main sequence secondary star with a rapidly spinning primary WD. The luminosity is higher than the stellar contributions alone, and is thought to be powered by the spin down of the WD. To date, only two such systems are known — AR Sco and eRASSU J191213.9−441044 — making them an exceptionally rare class of compact binaries. These systems are characterized by exhibiting strong pulsed emission across the entire electromagnetic spectrum (from radio to X-rays) associated with the spin period of the WD (Marsh et al. 2016; Stanway et al. 2018; Takata et al. 2018; Pelisoli et al. 2023; Schwope et al. 2023). One of the most distinctive observational features of WD pulsars arises from their optical light curve. In their monochromatic lightcurves, white dwarf pulsars exhibit an orbital modulation with a single maximum per orbital cycle, which suggests the presence of a hot component that is not directly detected in their optical spectra, this effect is reminiscent of post-common envelope systems hosting a hot white dwarf (e.g. NN Ser; Brinkworth et al. 2006; Aungwerojwit et al. 2007). In WD pulsars, however, the compact object is relatively cold (Garnavich et al. 2021; Pelisoli et al. 2024), therefore the heating of their companions should be negligible and their lightcurves should exhibit two maxima per orbital cycle (e.g. Gänsicke et al. 2004). This phenomenology suggests that the companion star in WD pulsars is heated by a different mechanism−likely the observed non-thermal emission. Unlike traditional accreting systems, whose short-term variability is dominated by stochastic "red" noise (e.g. Scaringi et al. 2015), the observed light curves of WD pulsars exhibit highly coherent pulses, signalling the absence of accretion onto the WD (Pelisoli et al. 2022b). The lack of significant mass transfer between the binary components is also supported by their optical/near-infrared spectroscopic properties and low X-ray luminosities. In particular, their observed spectra are dominated by the molecular bands typical of a relatively cold M-dwarf star with very narrow emission lines originating from its irradiated face (e.g. Garnavich et al. 2019).

At optical wavelengths, the pulsed emission can outshine the stellar components and exhibits a strong linear polarization, up to 40

★ E-mail: Noel.Castro-Segura@Warwick.ac.uk per cent with up to a 90 per cent pulse fraction in the WD pulsar prototype, AR Sco. These polarized components show periodicities consistent with both the spin period and the beat of the spin and orbital periods, suggesting that the emission is driven by the interaction of the WD's magnetosphere with the atmosphere of the stellar companion (Buckley et al. 2017). This is consistent with the location of energetic emission line flashes observed in AR Sco (Garnavich et al. 2019), however the mechanism behind the pulsing behaviour is still debated (e.g. Geng et al. 2016; Katz 2017; Takata et al. 2018; Potter & Buckley 2018; du Plessis et al. 2022; Barrett & Gurwell 2025).

Regardless of the details on how the pulsed emission is generated, WD pulsars are instrumental in our understanding of the formation and evolution of magnetic WDs. WD pulsars may be the missing link between the two main classes of accreting magnetic WDs, which represent a large fraction of interacting WD binaries (Pala et al. 2020; Rodriguez et al. 2025). These are known as polars and intermediate polars (a.k.a. AM Her and DQ Her stars respectively; e.g. Warner 1995), and they are distinguished by having spin and orbital period synchronised (polars) or asynchronous (intermediate polars), as a consequence of their relative difference in magnetic field strength with the orbital period, which can magnetically lock the orbit with the WD rotation (with typical magnetic fields strengths $B > 10$ MG for polars, and below that for intermediate polars). Schreiber et al. (2021) proposed an evolutionary scenario where the WDs in accreting binaries initially have weak magnetic fields, allowing for efficient accretion that spins up the WD primary. As they cool down and their cores starts to crystallize, the rapid rotation may trigger a dynamo, generating a magnetic field (e.g. Isern et al. 2017). The system then appears as an intermediate polar. As the field strengthens, magnetic coupling with the companion slows the WD's spin via transfer of angular momentum from the WD to the orbit, potentially detaching the system and producing a WD pulsar stage. Continued angular momentum loss will eventually bring the system into contact, thus restarting the mass transfer and evolving the system into a polar. It is important to note that the efficiency of the crystallisation dynamo originally incorporated in this model is under discussion, with recent works suggesting that it would not generate a strong enough magnetic field (Castro-Tapia et al. 2024; Camisassa et al. 2024). In any case, there is observational evidence that white dwarfs become more magnetic as they age (e.g. Bagnulo & Landstreet 2022), which is the necessary condition in the model. How compressional heating (Townsley & Bildsten 2004) might disrupt the magnetic field emergence is another aspect under consideration, given the estimated temperatures for the known WD pulsars of $\approx 11,500$ K (Garnavich et al. 2021; Pelisoli et al. 2024). Moreover, the recent identification of M-dwarf – WD binaries in some long-period radio transients (LPTs) suggests a possible evolutionary link to WD pulsars (Hurley-Walker et al. 2024; de Ruiter et al. 2025; Rodriguez 2025).

Despite their undisputed importance, a larger sample of WD pulsars must be identified in order to draw an evolutionary scenario. Here we present the discovery of the third system of this class, SDSS J230641.47+244055.8 (hereafter SDSSJ2306). We make use time-resolved spectroscopy and high-cadence photometry to determine the fundamental properties of this new system and compile the observational properties of all three known WD pulsars, providing a benchmark for the classification of future candidates.

Table 1. ULTRASPEC observing log.

Epoch	$\mathrm{MJD_{start}}$	filter	exposure time	obs. length
	day		second	hours
1	59926.499	$KG5$	7.8	3.52
2	59927.511	$KG5$	15.8	2.90
3	59928.487	$KG5$	7.8	3.62
4	60277.487	$KG5$	15.8	2.56

2 DATA SETS

2.1 Initial discovery data

SDSSJ2306 was classified as an EW-type contact binary with an orbital period of 6.988 h by Chen et al. (2020) from an analysis of the Zwicky Transient Facility (ZTF; Bellm et al. 2019a,b; Graham et al. 2019; Dekany et al. 2020) Data Release (DR) 2 photometry. Later, Inight et al. (2023) identified SDSSJ2306 as a cataclysmic variable (CV) candidate on the base of its Sloan Digital Sky Survey (SDSS; Blanton et al. 2017) spectrum, noting the dominant contribution of the companion star. As we show in Fig. 1, SDSSJ2306's spectrum gathered by SDSS exhibits strong narrow emission lines in the Balmer series overlaid on top of a relatively feature-less continuum in the blue-end. The red-end of the spectrum, on the other hand, is dominated by molecular bands characteristic of cold M-dwarf companions. This is one of the key characteristics observed in WD pulsars (see Sec. 4.1).

2.2 Time-resolved photometry

In data release 20 (DR20), The Zwicky Transient Facility (ZTF; Bellm et al. 2019a,b; Graham et al. 2019; Dekany et al. 2020) gathered long term photometry of SDSSJ2306 ranging from 2018/05/08 to 2023/10/25, yielding a total of 1473 individual exposures (436, 857 and 180 for g, r and i respectively). ZTF is a wide-field survey covering 47 deg^2 of the sky. It is mounted on the Samuel Oschin 48" Schmid telescope at Palomar Observatory. The nominal exposure time is 30 s, reaching a 5σ detection limit of 20.5 mag. We used this data to constrain the orbital period of the system (see Sec. 3.1.1). The folded light curve for the r band is presented in the top panel of Fig. 2.

We observed SDSSJ2306 with ULTRASPEC (Dhillon et al. 2014), a high-speed photometer mounted at the 2.4-m Thai National Telescope (TNT). ULTRASPEC is equipped with a 1024×1024 frame-transfer, electron-multitplying CCD (EMCCD) with a maximum field of view of 7.7×7.7 arcmin^2. We executed four visits to SDSSJ2306 during the nights of the 13, 14, 15 December 2022 and 29 November 2023 with exposure times of 8 s, 15 s, 8 s and 15 s respectively, with only 15 ms dead time between each exposure. All observations used a wide KG5 filter (effectively $u + g + r$; Hardy et al. 2017). A full log of the ULTRASPEC observations is listed in Table 1. The data were reduced using the `HiPERCAM` pipeline[1] (Dhillon et al. 2021). Prior to analysis, all the bad intervals due to poor weather conditions were removed and all the timestamps were centred to mid exposure and converted to the barycentric reference frame using `jpl` ephemerides by applying the methods implemented in `astropy.time` (Astropy Collaboration et al. 2018).

---

[1] https://github.com/HiPERCAM/hipercam

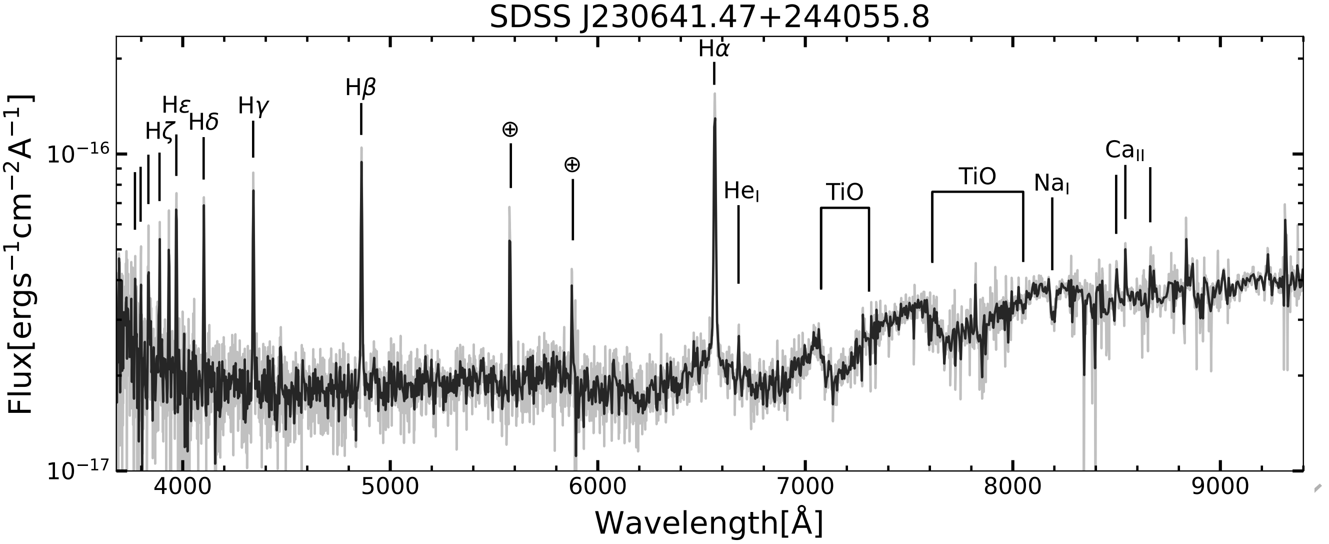

Figure 1. SDSS optical spectrum of SDSSJ2306. The unbinned and binned (by a factor of three) spectrum is shown in a light grey solid and black solid lines, respectively. The Balmer series is identified, superimposed on a relatively featureless continuum. At wavelengths longer than 6000 Å, the spectrum exhibits TiO molecular bands typical of an M-dwarf atmosphere; the lines in the red side of the spectrum that are studied in the present research are also labelled (i.e. H$_\alpha$, He λ6678 Å, the Ca II triplet ($\lambda\lambda$8498, 8542 & 8662 Å) and the 8190 Å Na I doublet. The SDSS identifiers of this spectrum are: MJD=57332, plate=7705, fiber=321.

2.3 Time-resolved spectroscopy

We obtained long-slit spectroscopy of SDSSJ2306 with the Gemini Multi-Object Spectrograph (GMOS; Hook et al. 2004) mounted on the 8-m Gemini North telescope (program ID: GN-2023B-Q-228). The GMOS instrument is equipped with two Hamatsu CCDs ($2 \times 2048 \times 4176$ pixels). Time-resolved spectroscopy was obtained in two visits during two different nights (on the 28th & 30th July 2023), yielding a total of 20 individual exposures. Each night, two consecutive observations (OBs) were performed, comprising one arc and four science exposures, designed to minimize the impact of flexures on the wavelength calibration. The exposure time ($t_{\mathrm{exp}} = 553$ s) was selected to be a multiple of the period of the high frequency signal to dilute any impact in the line profiles.

The observations were carried out with the R831 grating centred at 750 nm, 2×2 binning, and 1 arcsec slit width, providing coverage of H$_\alpha$, He λ6678, the 8190 Å Na I doublet, and the Ca II triplet ($\lambda\lambda$8498, 8542 & 8662 Å), with a resolving power $R \simeq 4400$, equivalent to a resolution of $\delta v \simeq 68\,\mathrm{km\,s^{-1}}$. The data was reduced using standard procedures using the latest version of the `DRAGONS` pipeline[2]. Barycentric correction was applied to the timestamps using the same method as above. The spectroscopic data were also corrected to the barycentric rest frame.

3 ANALYSIS AND RESULTS

3.1 Photometric monitoring

3.1.1 Orbital period

To characterise the long term variability of SDSSJ2306 we combined all the data available from ZTF to compute the multi-band generalized Lomb-Scargle periodogram (Lomb 1976; Scargle 1982; VanderPlas & Ivezić 2015; VanderPlas 2018) as implemented in `astropy` version 6.1.2. We obtain a clean detection of a signal $P \simeq 3.5$ h in the resulting power spectrum associated with the orbital period of the system. The data also showed a hint of a short period which further motivated the follow up. We determined the central frequency of the main signal and its uncertainty using a bootstrap analysis (e.g. Ivezić et al. 2014), resulting in

$$P_{\mathrm{orb}} = 3.4939558(3)\ \mathrm{h}.$$

Table 2. List of all the coherent signals extracted from ULTRASPEC data. ω is the strongest signal in the power spectrum which we associate with the spin period. Combinations of the beat between the orbital frequency Ω with ω are also identified.

Frequency (mHz)	Period (s)	Origin
10.836(3)	92.28(3)	ω
21.685(4)	46.11(1)	$2\,\omega$
21.853(5)	45.76(1)	$2\,\omega + 2\,\Omega$
32.62(2)	30.65(2)	$3\,\omega + \Omega$

Interestingly, this value is half of the period that triggered the classification as a contact binary by Chen et al. (2020). The long-term photometric (folded) light curves are presented in the top panel of Figures 2 and A1 for the r-band and gri-bands respectively. The orbital modulation from the companion star dominates the g and r bands as shown in these figures, as a result of an increase in the effective temperature of the companion star facing the WD, which is being heated by radiation, interaction of the magnetic fields from the two binary components, or both. (Sec.3.2). Superimposed on the orbital modulation, we can see a variable scatter with larger amplitude at specific orbital phases. These short term variations are intrinsic to the source, resembling the behaviour seen in AR Sco and J1912 (e.g. Marsh et al. 2016; Pelisoli et al. 2023).

---

[2] https://dragons.readthedocs.io/en/stable/

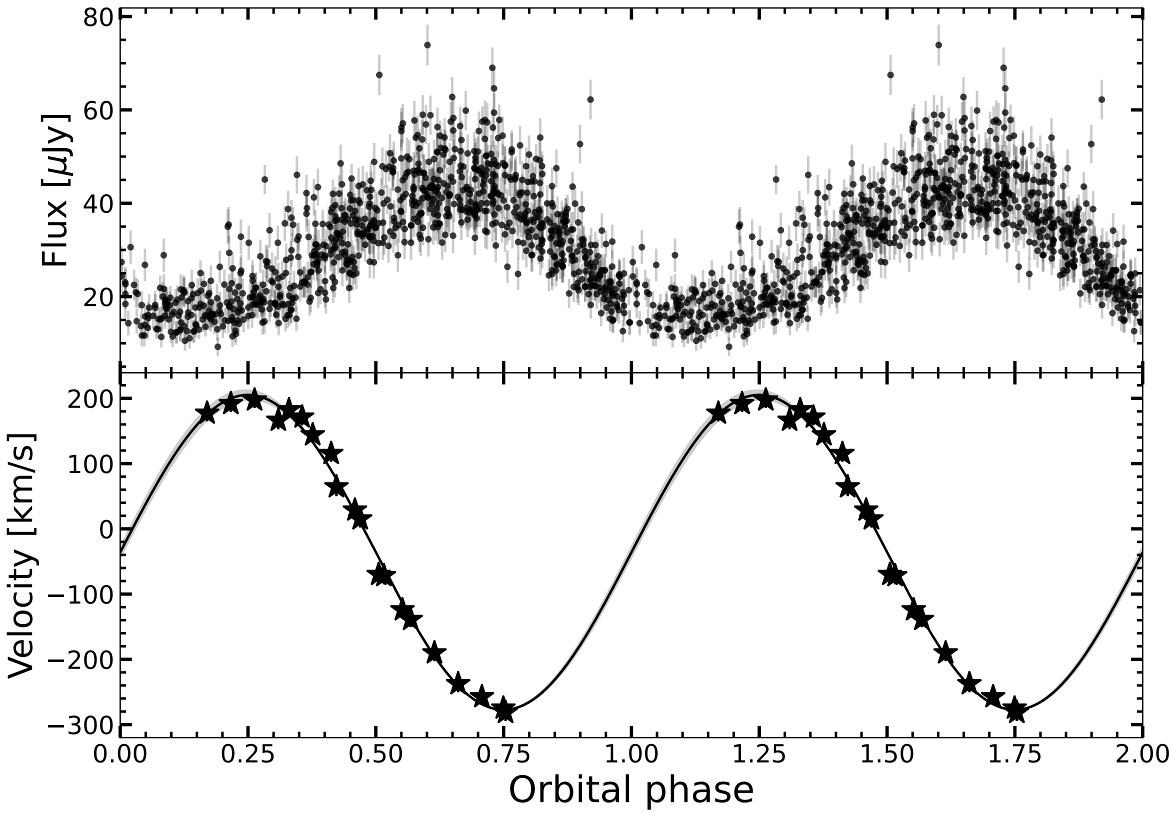

Figure 2. Optical flux and radial velocity curve of SDSSJ2306 as a function of the orbital phase. **Top:** ZTF optical light curve in the r band. The orbital modulation exhibits a large scatter at orbital phases when the trailing face of the companion star faces Earth similar to what is observed in AR Sco and J1912 (e.g. Marsh et al. 2016; Pelisoli et al. 2023). **Bottom:** Sinusoidal modulation of the Na I absorption lines tracing the orbital motion of the companion M star with a period of 3.49 h.

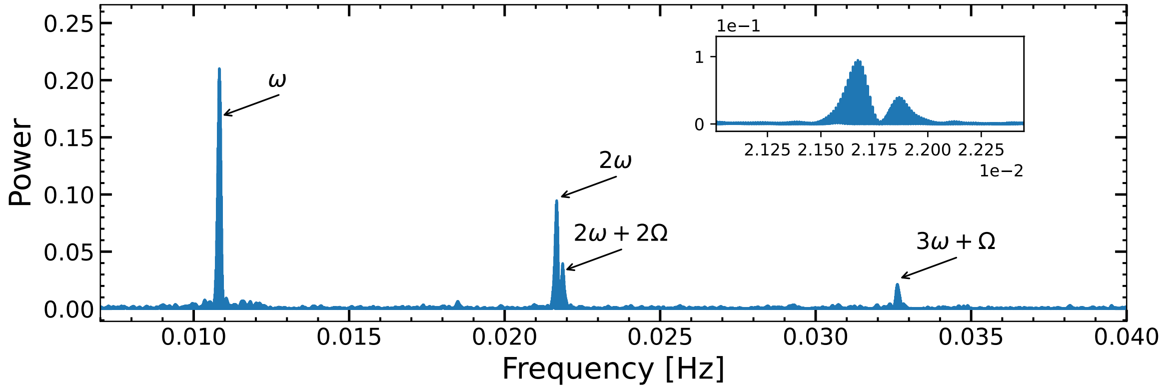

Figure 3. Power spectrum of the high cadence data obtained with ULTRASPEC (after removing the orbital modulation). The strongest signal is at $P_{\omega} \simeq 92$ seconds, the first harmonic of this signal is clearly identified, as well as the beat between the orbital period (Ω) and P_{ω}. The inset shows a zoom in around $2 \times \omega$ illustrating the excess of power on the beat period ($2\omega + 2\Omega$).

3.1.2 Spin period

We have used the fast photometry gathered with ULTRASPEC to determine the short-term properties of SDSSJ2306. To remove the orbital modulation before proceeding with any analysis, we de-trended the observed light curves using a sinusoidal function with the orbital frequency derived above. We then computed the Lomb-Scargle (LS) power for the combined time series and group by exposure times, fast ($t_{\rm exp}$ = 7.8 s) and slow ($t_{\rm exp}$ = 15.8 s). Finally, we determined the uncertainties for the main signals in each of these. The nights with longer exposures not only have slightly less accumulated exposure time but also less favourable weather conditions, yielding less precise results when these data are incorporated to the analysis, i.e. we recover the same frequencies with higher uncertainty. Thus, we only retain the higher cadence in our analysis. The resulting power spectrum is shown in Fig. 3, where we can see a dominant signal of

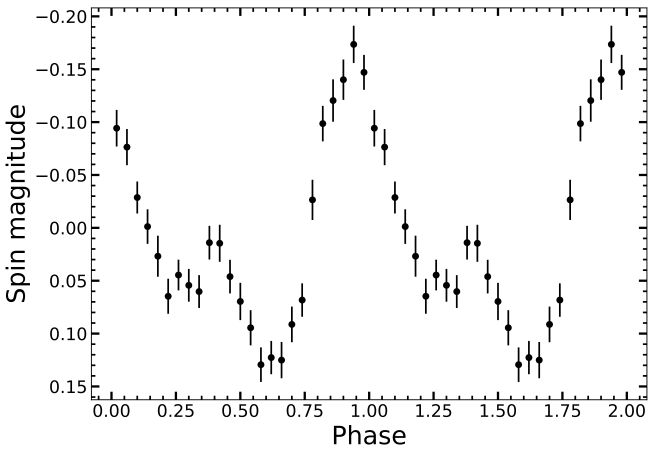

Figure 4. ULTRASPEC light curve of SDSSJ2306 folded on the $P_\omega \simeq 92$ s period. The orbital modulation was subtracted from the data before folding. The resulting light curve exhibits two distinct pulses per cycle, potentially owing to the change in the visibility of the near- and far-side poles of the WD. The spin phase ephemeris is arbitrary and two cycles are shown for clarity.

$P_\omega \simeq 92$ s, which we interpret as the spin of the WD producing the pulsed emission as the viewing angle of the WD changes and/or its magnetic field interacts with the companion star in each rotation, provided that is the only detected signal at low frequencies. We can also see some of its respective harmonics, as well as some of the beat periods between this signal (ω) and the orbital period. To determine the centroid and 1σ errors we followed the same bootstrapping method as in Sec. 3.1.1. The list of all the coherent signals detected in the high-speed photometry and their proposed origin are summarized in Table 2.

In Fig. 4 we show the light curve resulting from subtracting the orbital modulation folded into P_ω and rebinned. This figure reveals a double pulsed emission within one phase with a primary pulse amplitude of ~ 6 per cent. However, the intrinsic shape of the signal may have been distorted given the combination of low S/N with possible variations in amplitude and shape of pulsed emission with the orbital phase and on longer timescales (e.g. Pelisoli et al. 2022b). The modulation of the pulse amplitude induced by P_ω is seen in the upper panel of Fig. 2. To quantify this change, we separate the light curve (folded with $P_{\rm orb}$) into 10 segments, thus, covering $\Delta\phi_{\rm orb} = 0.1$ per segment. We perform a sinusoidal fit to each of these segments using the Simplex algorithm (Nelder & Mead 1965; Wright 1996) as implemented in `scipy` version 1.13.0. Using all the high-cadence data from ULTRASPEC, we obtain a typical peak-to-peak variability amplitude of $\lesssim 10$ per cent reaching a minimum amplitude of ~ 7 per cent variability during certain orbital phases. The signal to noise ratio of the fast photometry prevents us from quantifying these changes precisely, but qualitatively we can say that the dispersion decreases towards $\phi_{\rm orb} = 1$, i.e. when the trailing face of the companion star is on the far side, which is consistent with the spectroscopic modelling below.

3.2 Spectroscopic analysis

The time-resolved spectroscopy was obtained during two consecutive nights with a small gap during the first visit and partial overlapping of the orbital phase. In Fig. 5 we show the trailed spectra of all the lines of interest, namely H_α, He λ6678 Å, the Ca II triplet ($\lambda\lambda$8498, 8542 & 8662 Å) and the 8190 Å Na I doublet. In this section we present an in-depth analysis of the spectroscopic properties of SDSSJ2306. For our analysis we have used the spectroscopic data binned to two pixels per resolution element determined by the resolving power of our instrument setup (i.e. $R \simeq 4400$).

3.2.1 *Line Modelling & Orbital Ephemerides*

From Fig. 5 it is clear that SDSSJ2306 is a spectroscopic binary as it exhibits S-waves in the Hydrogen and Helium lines, as well as the Calcium triplet in emission. These are typical signatures observed from the inner face of companion stars owing to the temperature inversion in their surface due to the heating caused by the compact object or magnetic reconnection (e.g. Haefner et al. 2004; Garnavich et al. 2019).

To obtain the radial velocity curves of the emission lines, we modelled the centroid of the lines. We performed all the fits to the continuum-subtracted spectra using models implemented in `astropy` and carrying out Markov chain Monte Carlo (MCMC) with a Goodman & Weare's Affinite Invariant Ensemble sampler as implemented in EMCEE[3] (Astropy Collaboration et al. 2018; Foreman-Mackey et al. 2013). For each line, we first modelled the underlying continuum using a second order polynomial fitted to the neighbouring regions where contribution from the lines is negligible. The lines were modelled using Gaussian profiles with an added constant, to avoid bias owing to over/under estimation of the continuum at the line centre. Simple non-informative uniform priors were adopted for all fit parameters. To produce the MCMC chains we used 100 walkers per free parameter and ran them until the chains were sufficiently converged, i.e. until the chain number of iterations was at least 100× the auto correlation time (τ) and the latter did not improve more than 1 per cent after 500 iterations. The first $2\times\tau$ iterations were discarded and the chains were thinned by segments of $\tau/2$ to minimise the effect of auto-correlation from the sampler. For all the fits, the resulting posterior distributions exhibit roughly normal distribution for all the parameters. The best fitted values are drawn from the posterior probability distributions of each parameter with the uncertainties drawn from the 16 per cent & 84 per cent quantiles of the sampled posterior.

In the case of Hα and He I, a single Gaussian component does not provide a good fit to the line profile in most cases. This is due to the influence of a broad base which is seen in the median spectra of Fig. 5. We attempted to fit the profiles with two Gaussian components, however, this resulted in poorly constrained and unphysical values, even when forcing the centre of one of the narrower components to the centroid of the emission core fitted with a second order polynomial. Therefore, we limited our analysis of Hα and He I to determining only the centroid of the narrow emission by fitting a second order polynomial to the maximum of the line. In this case, we determined the error on the lines by bootstrapping each wavelength bin assuming Gaussian errors determined from the adjacent continuum. On the other hand, the Ca triplet emission lines are not resolved with our spectral resolution. The triplet was fitted with its full width at half maximum (FWHM) tied to a single value in each epoch. However, the radial velocity was required to have some degree of freedom to accommodate the fit in some of the individual exposures due to the systematics introduced during the wavelength calibration. Finally, we modelled the Na I absorption doublet at $\lambda\lambda = 8150, 8224$ Å, shown in the right panel of Fig. 5. In this case, we used two Gaussians with

---

[3] https://github.com/dfm/emcee

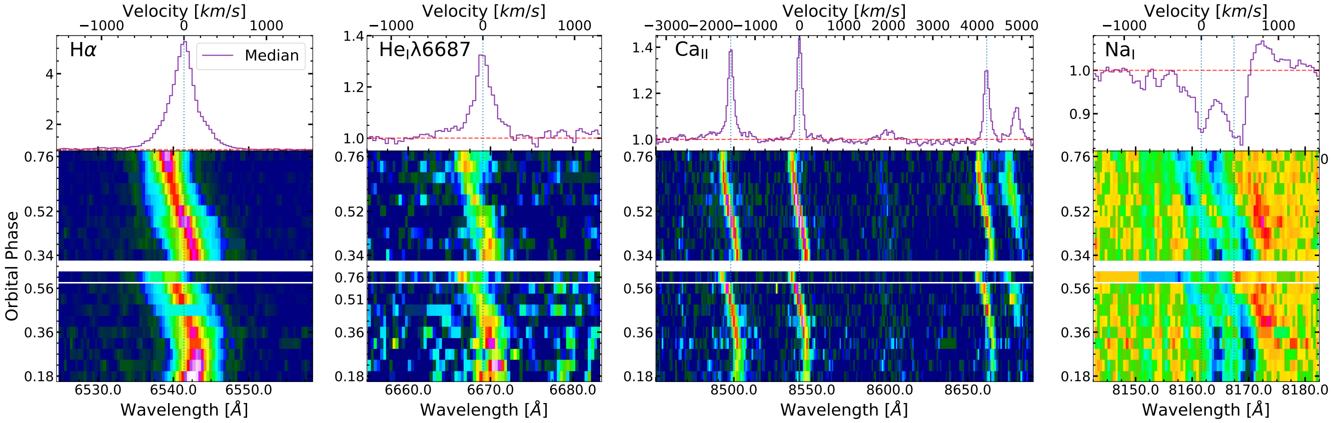

Figure 5. Trailed spectra of the spectral lines analyzed in the present research. From left to right: H$_\alpha$, He I λ6678, Ca II triplet (λλ8498, 8542 & 8662 Å), and the 8190 Å Na I doublet. The top panels show the rest-position median spectrum for each line. The bottom panels show the time-resolved trailed spectra for the two sets of observations separated by a horizontal white space after $\phi_{\rm orb} = 0.76$, the horizontal line in the bottom set indicates a gap in the sequence, the specific orbital phase for the last observation of that set is 0.76. The typical phase difference between consecutive exposures is $\Delta\phi = 0.046$. In these panels the intensity is colour coded as dark blue corresponding to the minimum and light magenta to the maximum. Note that some of the individual exposure have masked pixels due to the impact of cosmic rays in the CCD during the exposure.

FWHM tied to the same value and the distance between them was fixed to their laboratory separation.

In order to determine the time 0 ephemerides (T_0) of SDSSJ2306, defined as the inferior conjunction of the companion, we perform a sinusoidal fit to the centroid of each ionisation species with an expression of the form:

$$v_i(t) = \gamma_i + K_i \sin\left(2\pi(t - T_0)/P_{\rm orb}\right), \tag{1}$$

where $v_i(t)$ and K_i are the observed velocity and its amplitude for the i-th ionisation species. γ_i is the systemic velocity of such species, and P$_{\rm orb}$ is the orbital period determined from the long-term photometric light curves (Sec. 3.1.1).

The radial velocity measurements for each spectroscopic line along with the the best fits to equation 1 are shown in Fig. 6, and in the bottom panel of Fig. 2 for Na I. The fit was performed using the MCMC technique described above, and the best fitted values and uncertainties are reported in Table 3. In this case, the uncertainty in the orbital period was modelled as a Gaussian distribution, with both the mean and standard deviation treated as a hyperparameter in the MCMC chains. A total systematic error ($\sigma_{\rm sys}$) was also introduced in the likelihood function as a free parameter to capture errors introduced by small offsets in the wavelength solution during the data reduction, so the uncertainty for the n-th radial velocity measurement can be written as $\sigma^2_{\rm T,n} = \sigma^2_n + \sigma^2_{\rm sys}$. We have estimated the T_0 ephemerides for each of the lines and the combination of them resulting in consistent values for all of these. Given the uncertainties introduced by the low S/N on He I, and the fact that in some of the epochs Hα are affected by cosmic rays, here we report the ephemerides with the least uncertainty obtained from the calcium triplet:

$$\mathrm{T}_0^{\rm Ca\,II}(\mathrm{MJD_{TDB}}) = 60154.2911(4) + 0.14558149(1)\mathrm{E}.$$

Table 3. Best-fit values and uncertainties for the radial-velocity fits from equation 1, as shown in Fig. 6. $\sigma_{\rm sys}$ is the total systematic error added to the likelihood function. The posterior distributions are nearly Gaussian; therefore, only symmetric errors are reported. Times are in MJD$_{\rm TDB}$, with an offset of 60154 subtracted.

	K km s^{-1}	γ km s^{-1}	$T_0 - 60154$ d	$\sigma_{\rm sys}$ km s^{-1}
Ca II	164.0(18)	−24.0(23)	0.29117(43)	7.1(9)
Hα	167.8(44)	−32.4(50)	0.2925(10)	13.5(26)
He I	156.3(79)	−47(11)	0.2946(20)	$\sim 0^{\dagger}$
Na I	241.3(40)	−36.0(45)	0.29240(62)	10.4(30)

† The uncertainty (0.13) is orders of magnitude larger than the value (4.12×10^{-5}) due to poor S/N in many of the spectra (c.f. Fig 5).

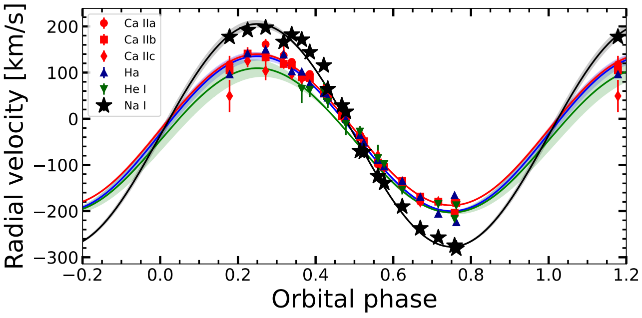

Figure 6. Radial velocities folded with the orbital phases. Each symbol corresponds to an absorption or emission line measured from the time resolved GMOS spectroscopy. The solid line is the best sinusoidal fit to each ionisation species and the shaded regions represent the ±1σ error on the fit. Error bars in Na I are smaller than symbols.

3.2.2 The Companion Star & Mass Function

As shown in Fig. 1, the red spectrum of SDSSJ2306 unambiguously identifies the companion as an M-dwarf, exhibiting molecular bands characteristic of these late-type stars. Our time-resolved spectroscopic observations are designed to cover this spectral region (spanning $\lambda \simeq 6320-8700$Å), which contains key information about the stellar component in the binary system. The sodium doublet is particularly important as it approximately traces the centre of mass of the companion star. It is worth noting that the centre of light for the sodium doublet can be offset by the difference in temperature difference between the star's hemispheres (c.f. Friend et al. 1990). Our data is not exempt from this effect, as evidenced by the weakening of the absorption feature around phase 0.5 in Fig. 5, which makes our constrains on K_2 effectively an upper limit. However, since the best-match template does not change with the orbital phase (see below), the impact of this effect in our case must be small and is likely dominated by other sources of systematic error. With this in mind, we use the semi-amplitude of the Na I line to constrain the binary mass function of the system ($f(M_1)$, following the same approach as Marsh et al. 2016 and Pelisoli et al. 2023). The mass function can be written as

$$f(M_1) = \frac{M_1^3 \sin^3 i}{(M_1 + M_2)^2} = \frac{K_2^3 P_{\rm orb}}{2\pi G} \qquad (2)$$

where $P_{\rm orb}$ is the orbital period, K is the radial velocity semi-amplitude tracing the centre of mass of the donor, G is the gravitational constant, i is the orbital inclination, M_1 and M_2 are the mass of the primary and the secondary respectively. Combining the values obtained above we obtain $f(M_1) = 0.21 \pm 0.01\,{\rm M}_\odot$, where we used $K = K_{\rm Na\,I}$.

The Na I line is also very sensitive to the effective temperature of the stellar atmosphere and hence to its spectral type. The presence of this line itself implies an M-dwarf companion. To infer the spectral type, we have compared our GMOS data against a set of well-characterised M-dwarf spectral templates presented in Parsons et al. (2018). The best match was determined by computing the χ^2 of the red-end spectrum dominated by the M-dwarf, using only regions free from either telluric or emission lines[4]. Prior to the comparison we de-reddened all the individual spectra using the Fitzpatrick (1999) extinction law as implemented in `dust_extinction`[5] v1.5. The extinction was determined using the 3D maps from Green et al. (2019), these maps reveal a constant extinction of $E(g-r) = 0.23 \pm 0.02$ in the line of sight throughout the region populated with stars (i.e. from $\simeq$ 0.5 kpc to $\simeq$ 6.5 kpc). $E(B-V)$ was derived using the values tabulated in Table 6 of Schlafly & Finkbeiner (2011) and $R_V = A_V/E(B-V) = 3.1$ (e.g. Savage & Mathis 1979). We then centred the observed spectra in the donor rest frame using the radial velocities from Sec. 3.2. To account for other spectral components that may influence the shape of the underlying continuum, we fitted each template to the observed spectra with a veiling component emulating the non-thermal emission which is represented by a power law (using least squares fits as implemented in `astropy`). The data is best described by a M2.5 spectral type, for the median spectrum as well as the individual exposures. This value is earlier than the M4.5 spectral type observed for other WD pulsars and may be underestimated due to the lack of spectra at 0 orbital phase. To test this further, we have repeated the same experiment using the SDSS spectrum shown in Fig. 1. Using this data, the best match is obtained for the M4 with similar values for M3 and M5, with the latter being slightly better of than M3. These values are a more natural match for SDSSJ2306's orbital period and are consistent with fact that all three WD pulsars are clustered in the same region of the colour magnitude diagram (see Sec. 4.1). Therefore, we conclude that the most likely spectral type of SDSSJ2306 is M4.0 ± 0.5. From the individual fits of the GMOS data, it is also clear how the veiling factor changes in each orbital phase. Even though we do not cover all the orbital phases, in these fits the veiling factor decreases rapidly from $\phi_{\rm orb} \simeq 0.17$ finding a minimum around $\phi_{\rm orb} \simeq 0.6$, consistent with the phase dependent scatter from the light curve estimated in Sec. 3.1.2.

Table 4. System parameters of SDSSJ2306. † indicates estimates derived assuming that the average luminosity in the Gaia G-band is similar to the one from AR Sco and adopting the semi-empirical mass-radius relation from Brown et al. (2022), see Sec. 3.4 for details.

Parameter	value (error)	units
$P_{\rm orb}$	3.4939558(3)	h
$P_{\rm spin}$	92.28(3)	s
Spectral type	M4.0 ± 0.5	
$T_{\rm eff,2}$	3300(100)	K
$\log_{10}(R_2/d)^2$	-21.95(6)	
$f(M)$	0.21(1)	M$_\odot$
$M_2^\dagger$	0.19 – 0.28	M$_\odot$
$d^\dagger$	1.2(2)	kpc

By subtracting the non-stellar continuum from the best fitted template, we can obtain a good estimation of the stellar flux that can be used to further characterize the stellar component. We used the grid of stellar M-dwarf models from Allard et al. (1997) to compute the maximum likelihood function of the effective temperature ($T_{\rm eff,2}$), and the normalization factor $\log_{10}(R_2/d)^2$, where R_2 and d are the radius of the stellar companion and the distance to the system respectively. We obtain the most likely values and their equivalent 1σ uncertainties to be $T_{\rm eff} = 3600 \pm 100$ K and $\log_{10}(R_2/d)^2 = -21.73 \pm 0.06$. We note that a lower temperature would be more typical for this class of system and spectral type, we suspect that it may have been slightly overestimated for the same reasons discussed above. Repeating the same logic as with the spectral type classification, we find that an effective temperature of 3500 K have the most likelihood, however $T_{\rm eff} = 3300 \pm 100$ K lead to similar χ^2 while being consistent with the value quoted above and providing a more natural match to the spectral class. All the values are summarised in Table 4.

3.3 Constrains from Roche geometry

The radial velocities of the lines observed in 3.2 allow us to obtain further information about the properties of the system. For an irradiated companion filling its Roche lobe in a close binary, the narrow emission lines typically originate in the irradiated face lying very close to the inner Lagrangian point. Therefore, the amplitude of their observed radial velocity curves (K') is modulated by the projected geometry of the secondary's Roche lobe, i.e. the "true" semi-amplitude tracing the centre of mass of the secondary $K = K(K', q, i)$, is a function of the mass ratio of the system q, and the inclination of the system which affects the geometrical projection towards the observer. The effect on the mass ratio is known as the $K-$correction (e.g. Muñoz-Darias et al. 2005), and it can be a very powerful tool to constrain fundamental parameters of binary systems. In the case of SDSSJ2306 we also detect narrow absorption lines originating in the cold atmosphere of the companion star. These lines, namely Na I, are a good tracer of the centre of mass of the secondary star (e.g. Marsh et al. 2016, but also see Friend et al. 1990). The effect of the $K-$correction is already noticeable in Fig. 6, here we can see how all the lines share the same systemic velocity (γ) and orbital period, however the amplitude of the absorption line ($K_{\rm Na\,I}$) is much larger than the one from the measured emission lines.

As we show in the left panel from Fig. 7, the geometrical effect induced by the $K-$correction can be easily visualized by projecting

---

[4] i.e. excluding $\lambda\lambda$ = 6310 − 6600, 6664 − 6690, 7088 − 7118, 7348 − 7410, 7587 − 7742, 7886 − 7918, 8460 − 8700Å.

[5] https://dust-extinction.readthedocs.io

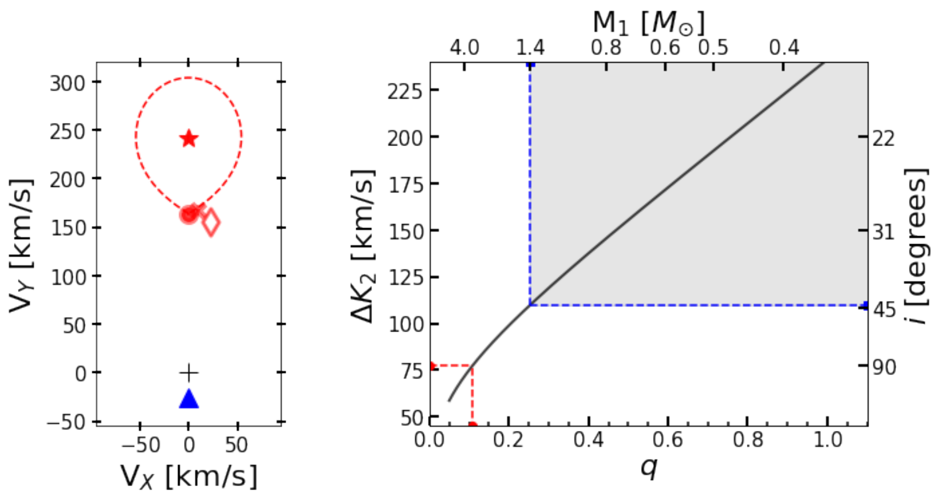

Figure 7. Left: projected velocities in the orbital plane V_x, V_y for the lines derived from our GMOS spectroscopy. The star indicates the centre of mass of the M-dwarf as estimated from the Na I radial velocity curve. H_α, He I λ6678 and the Ca II triplet are indicated with a red cross, a diamond and a circle respectively. The black cross and blue triangle are the centre of mass of the system and the WD respectively. The dashed red line is the Roche lobe of the companion for a mass ratio q = 0.11. While H_α, and Ca II have a broadly consistent position in the side of the companion facing the compact object, the He I line (open diamond), seems to be lying in the trailing face of the companion, probably owing to poor S/N at some specific orbital phases. This line was not included to determine the limit in the mass ratio $q_{\rm min}$. **Right:** The solid black line indicates the radial velocity difference (ΔK_2), between the irradiated face and the centre of mass of the secondary as a function of the mass ratio q for a Roche lobe filling companion star. The left y-axis is the maximum ΔK_2 for a given mass ratio. The right y-axis represents the required inclination to explain the observed ΔK_2 given by $K_{\rm Na\,I} - K_{\rm Ca\,III}$. The top x-axis represents the mass of the primary if we assume that the companion has the maximum density possible for this orbital period. The red dashed lines indicate the mass ratio for a system with $i = 90^{\rm o}$ with the observed ΔK_2 corresponding to q = 0.11. The blue dashed lines indicate the maximum inclination allowed for $M_1 = 1.4 {\rm M}_\odot$ and $M_2 = M_2^{\rm max}$, leading to the constrains $i \lesssim 45^{\rm o}$ and $q \gtrsim 0.25$ indicated by the shaded area.

the velocities studied in Sec. 3.2 into the V_x,V_y plane[6]. In this panel, the emission lines (big red symbols) lie close to the projected Roche lobe surface of the companion star of a system seen edge-on (red dashed line), i.e. a system with inclination $i = 90^{\rm o}$. Provided that the companion, and therefore the emission line region, has to be contained within its Roche lobe, the minimum mass ratio required to engulf the emission lines sets a lower limit for the mass ratio. In the case of SDSSJ2306 we find that the projected velocities of H_α, and Ca II have a broadly consistent position in the irradiated face of the companion, while the He I line lies in the trailing face of the companion, likely owing to poor S/N at some specific orbital phases (c.f. Fig. 6). Ignoring the position of He I in the diagram, we find that the mass ratio must be $q \gtrsim 0.11$. This lower limit in the mass ratio ($q = 0.11$), produces the Roche lobe shown by the red dashed line in the left panel of Fig. 7.

The black line in the right panel of Fig. 7, represents the $K-$correction ($\Delta K_2 = K_{\rm Na\,I} - K_{\rm Ca\,III}$) as a function of the mass ratio (q; left and bottom axes, respectively), for a Roche lobe filling companion star as seen at $90^{\rm o}$ degrees. Using this lower limit in the mass ratio we can recast the mass function (eq. 2) as $M_1 = f(m)\,(1+q)^2/\sin^3 i$, to obtain a lower limit on the primary and secondary masses, yielding $M_1 > 0.26\,{\rm M}_\odot$ and $M_2 > 0.028\,{\rm M}_\odot$.

The orbital period of the system also allow us to set an upper limit for the mass of the secondary. For a Roche lobe filling companion star, the maximum mean density it can have in g cm^{-3} is $\rho_2^{\rm max} = (0.43/P_{\rm orb})^2$, with $P_{\rm orb}$ in days (Eggleton 1983). Assuming the semi-empirical mass-radius relation from Brown et al. (2022) we obtain an upper limit for the mass of the secondary of $M_2^{\rm max} = 0.36\,{\rm M}_\odot$. The Brown et al. (2022) relation should correct the over-sized problem of companion stars in close binaries (e.g. Knigge et al. 2011). Therefore, we consider $M_2^{\rm max}$ as (or close to) the face value for mass of the companion star. With this assumption we can obtain a family of solutions compatible with the observed ΔK_2 as a function of the inclination and mass ratio. The former is the solid black line shown in the right panel of Fig. 7, the corresponding inclination is shown in the right y-axis of this figure, the top x-axis in this figure shows the corresponding primary mass that would explain the observed ΔK_2 provided $M_2 = M_2^{\rm max}$. This allows us to set a tighter constraint on the minimum mass ratio of the system that would be compatible with the observed K-correction and having a WD as the compact object (see Sec. 4.1 for a discussion on the nature of the compact object). In turn, the Chandrasekar limit will then provide a lower limit for the inclination of the system compatible with the observations, $i \lesssim 45^{\rm o}$, leading to the shaded region in this figure indicating the allowed region of the parameter space. This inclination is in agreement with the maximum inclination required for the system to be a non-eclipsing binary.

In short, the constrains on M_2 set by the orbital period of the system combined with the maximum $K-$correction required to explain the observed ΔK (assuming a Roche lobe filling donor), sets the maximum inclination and mass ratio allowed for a primary mass $M_1 \leq 1.4\,{\rm M}_\odot$ to be $i \lesssim 45^{\rm o}$ and $q \gtrsim 0.25$ respectively.

3.4 Distance to SDSSJ2306

SDSSJ2306 is detected in *Gaia* Data Release 3 (DR3) with the ID: DR3 2842721961392797312 (Gaia Collaboration et al. 2023). Unfortunately, the parallax is poorly constrained ($\pi \simeq 0.9 \pm 0.5$ m.a.s.). However, the target is listed in the Bailer-Jones et al. (2021) catalogue, with an estimated (geometric) distance of $d \simeq 1.5^{+1.5}_{-0.5}$ kpc. We

---

[6] Where V_x and V_y were obtained from the radial velocity expressed as $V = \gamma - V_x \cos(2\pi\phi_{\rm orb}) + V_y \sin(2\pi\phi_{\rm orb})$

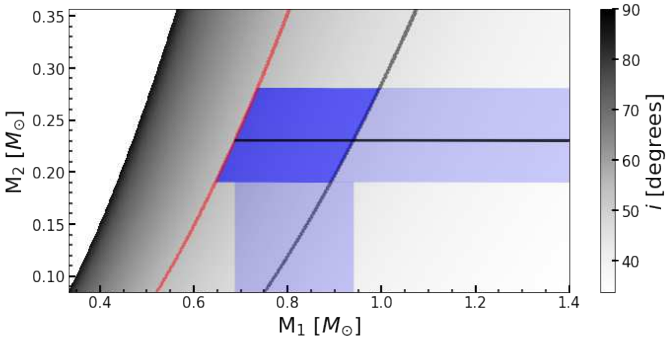

Figure 8. Mass of the primary vs secondary; the grey gradient is the corresponding inclination for each combination of masses determined from the mass function obtained in Sec. 3.2.2. The curves represent the maximum inclination for the system to be eclipsing ($i \lesssim 55^{\rm o}$, red curve on the left side) and the maximum inclination allowed for $\rm M_2 = M_2^{max}$ (black curve). The horizontal light blue region is the allowed secondary mass range compatible with our observations. The horizontal black line is the mass derived from the spectroscopic contribution of the donor at 1.2 kpc which fills ~ 90 per cent of its Roche lobe (see Sec. 3.4 for a discussion on the distance). The intersection of this mass range and the highlighted inclinations defines the vertical light blue region. This latter region is almost centred on the canonical mass of interacting WD binaries (e.g. Zorotovic et al. 2011; Pala et al. 2017). A hard limit of $M_1 \gtrsim 0.65\,\rm M_\odot$ can be set from this relation.

can further constrain the distance by combining the estimations of the distance modulus obtained in Sec. 3.2.2 with the mass-radius relation from Brown et al. (2022). We find that for a typical configuration of Roche lobe filling semi-detached binaries within the observed range of parameters ($0.25\,\rm M_\odot < M_2 < 0.35\,\rm M_\odot$ and $P_{\rm orb} \approx 3.5\,h$; Knigge et al. 2011) we find 1.3 kpc < d < 2.0 kpc. In fact, if the mass configuration of SDSSJ2306 is similar to J1912 (i.e. $M_2 \simeq 0.25 \pm 0.05\,\rm M_\odot$; Pelisoli et al. 2024), we obtain 1.1 kpc < d < 1.7 kpc, which is well in line with the distance from Bailer-Jones et al. (2021). Given the similarities of the observational properties of SDSSJ2306 with AR Sco (Sec. 4.1) we can assume both sources have the same luminosity and make a direct comparison using the average *Gaia* magnitude to obtain an estimate of the distance. Adopting the value from Gaia Collaboration et al. (2023) we have a distance of d = 117 ± 0.5 pc and $G_{\rm AR\,Sco}$ = 14.98(3) mag for AR Sco, and $G_{\rm J2306}$ = 19.9(2) mag for SDSSJ2306. We tested the impact of the spectral type (between M4 and M5) by applying synthetic photometry in the *Gaia* G band and found differences comparable to the photometric uncertainty of SDSSJ2306. A direct comparison of the magnitudes yields a distance of $d \simeq 1.1 \pm 0.1$, kpc, while accounting for extinction gives $d \simeq 0.85 \pm 0.10$, kpc. Considering the caveats associated with our assumptions and the limits from Roche geometry discussed above, we adopt a distance to SDSSJ2306 of $d \simeq 1.2 \pm 0.2$ kpc. Combining this value with the constrains from above, we obtain $0.19\,\rm M_\odot \lesssim M_2 \lesssim 0.28\,\rm M_\odot$ for Roche lobe filling factors ≥ 0.8, which is very similar to the constrains for J1912.

In figure 8 we show the relation between the primary and secondary masses with the inclination derived from the mass function obtained in Sec. 3.2.2. If we impose the condition that SDSSJ2306 is not an eclipsing system, we find a lower limit on the WD mass of $M_1 \gtrsim 0.65\,\rm M_\odot$. Interestingly, the intersection of the mass corresponding to a donor filling 90 per cent of its Roche lobe is centred around the canonical mass of WDs in interacting binaries (i.e. $M_{\rm WD} \approx 0.8\rm M_\odot$ e.g. Zorotovic et al. 2011; Pala et al. 2017), suggesting that the inclination of SDSSJ2306 is relatively high ($i \sim 50^{\rm o}$).

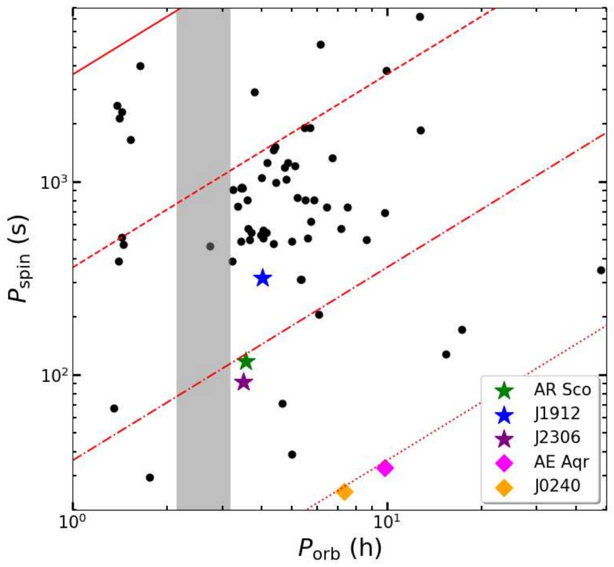

Figure 9. Spin period vs orbital period of confirmed IPs (back dots). Known WD pulsars and propeller systems are represented with coloured stars and diamonds respectively. The vertical gray area indicates the period gap, where there is a dearth of systems, as defined in Knigge et al. (2011). Diagonal lines correspond to spin periods of 1, 10, 100 and 1000 times the orbital period (solid, dashed, dash-dot and dotted line respectively). The most extreme systems are the propeller AE Aqr and LAMOST J024048.51+195226.9 with $P_{\rm spin}/P_{\rm orb} \simeq 10^3$. The WD pulsars AR Sco and SDSSJ2306 are clustered around $P_{\rm spin}/P_{\rm orb} \approx 10^2$, while J1912 lies much closer to the bulk of the IP population. Adapted from Mukai (2017).

4 DISCUSSION

4.1 The nature of the compact object in SDSSJ2306: defining the observational properties of WD pulsars

In section 3 we clearly identify SDSSJ2306 as a spectroscopic binary with a $T \approx 3300$ K M-dwarf companion harbouring a rapidly spinning compact object. But, what is the nature of the compact object? Given all the similarities with the known WD pulsars exposed throughout this research, the most natural interpretation is that the compact object is a WD where the short-term pulsations seen at P_ω are produced by the interaction of its magnetic field with the companion star's own field. In fact, the pulsed emission profile shown in Fig. 4 is very similar to that of AR Sco (see fig 2. from Marsh et al. 2016), with the spin (or beat) period almost identical to the WD pulsar prototype. If the pulsed emission is the actual spin period of SDSSJ2306, or even the beat period between the orbit and the spin (which would be about 10 per cent larger than the spin period), the rotation frequency of the compact object in SDSSJ2306 would be at least a factor of ten slower than the typical periods of magnetars, which are the slowest-rotating type of observed neutron stars (e.g. Rea et al. 2024). Even if we consider SDSSJ2306 as a magnetar, it should be a very young system, a scenario that does not match with the (likely) old M-dwarf companion (Beniamini et al. 2019), and the low X-ray luminosity implied by the non-detection by *ROSAT* (see below). Therefore, we can rule out the possibility of SDSSJ2306 harbouring a neutron star. In the remainder of this section we will summarize all the similarities with AR Sco, J1912 and SDSSJ2306,

Table 5. Summary table of White Dwarf Pulsars properties

		Observational properties of WD pulsars						
		Heated M-Dwarf [†]	No steady accretion [‡]	Pulsed emission [★]			↑ Optical Polarization [*]	↑ P_{spin}/P_{orb} [§]
				X-ray	OPT/NIR	Radio		
Target	AR Sco	✓	✓	✓	✓	✓	✓	✓
	J1912	✓	✓	✓	✓	✓	✓	✓
	J2306	✓	✓	?	✓	✓?	?	✓

[†] The large amplitude modulation ($\sim$ 1.5 mag) observed in the optical ligtcurves exhibiting one maximum per orbital cycle suggest the presence of a hot object. However, their spectrum does not show signatures of a hot WD, contrary to post-common envelope or sdB WD + M-dwarf binaries (e.g. Parsons et al. 2010; Schaffenroth et al. 2023).

[‡] The low X-ray luminosity, absence of flickering in the light curves, extremely narrow emission lines, and relatively cool white dwarf all indicate a lack of persistent accretion.

[★] Pulsed non-thermal emission across the electromagnetic spectrum is one of the characteristic of WD pulsars. The amplitude of these pulses is modulated with the orbital period.

[*] In AR Sco and J1912, the pulsed emission exhibits significant polarization degree at optical wavelengths. Reaching up to $\sim$ 40 per cent polarisation degree and a polarisation fraction of the pulsed emission near to 90 per cent in AR Sco (Buckley et al. 2017; Potter & Buckley 2018).

[§] In general WD pulsars have $P_{\rm spin}/P_{\rm orb} \sim 10^2$, which is larger than the typical observed in IPs, but less than the magnetic WD-propellers (see Fig. 9).

and identify the common properties that define WD pulsars. All these properties are summarized in Table 5.

One of the most distinctive observational properties of WD pulsars arises from their orbital modulation in the optical and the presence of minute-timescale pulses in their light curves. The short timescales are dominated by pulsed emission (see e.g. Fig. 4), contrary to accreting systems harbouring a magnetic WD (i.e. polars and intermediate polars) and there is no evidence of stochastic variability (a.k.a. flickering; Scaringi et al. 2015) signalling the lack of accretion. This pulsed emission is highly coherent and its amplitude is modulated with the orbital period, exhibiting maximum dispersion between orbital phases $\phi_{\rm orb} \sim 0.25 - 0.75$, associating the visibility of the emission region with the trailing inner face of the companion (i.e. L1). As shown in Fig. 9, the compact object of WD pulsars is spinning quite rapidly, $P_{\rm spin} \sim 10^2 \times P_{\rm orb}$. This is significantly faster than the bulk of the intermediate polars, but still a factor of ten slower than the known WD propellers (i.e. AE Aqr and LAMOST J024048.51+195226.9; Schenker et al. 2002; Pelisoli et al. 2022a, i.e. systems where mass transferred from the companion is accelerated and flung away from the system by the magnetic field of the fast-spinning WD). In addition to this the fast rotating IPs ($P_{\rm spin} \lesssim 10^2$ s) with orbital periods $P_{\rm orb} \lesssim 10$ h are classified as low luminosity systems (e.g. Joshi 2025), perhaps suggesting a common evolutionary scenario for rapidly spinning interacting WD binaries.

On longer timescales (hours) WD pulsar's light curves exhibit a $\sim$ 1.5 mag modulation with a single maximum per orbit, this is typically observed in detached systems harbouring a hot stellar remnant, where the surface of the companion star is heated by the strong radiation field from the primary (e.g. Brinkworth et al. 2006). However, the maximum of the light curve is not aligned either with quadrature or conjunction of the system as revealed by the spectroscopic orbital solution. This suggests a non-axi-symmetric origin of the heating mechanism, in line with the modulation of the pulsed emission. In addition to this, one would expect to observe the hot compact object heating the surface of the companion star, however, the blue part of the optical spectrum is clearly dominated by strong narrow emission lines superimposed on a featureless blue continuum (Fig. 1), implying a dominant non-thermal emission at short wavelengths. In this region, the Balmer emission series are the dominant lines observed, with a weak contribution of He I λ6678 Å and even weaker He II λ4686 Å. In SDSSJ2306 there is no actual evidence of He II λ4686 Å, which is particularly strong among accreting systems with rapidly spinning compact objects (e.g. Voikhanskaya 1987). All the core emission lines observed in WD pulsars are very narrow, to the point that we cannot resolve them in our Gemini/GMOS data for SDSSJ2306, implying in our case a FWHM $\lesssim 70\,{\rm km\,s^{-1}}$, another piece of evidence signalling the absence of mass transfer from the low mass companion onto the primary. The red end of the spectrum is dominated by molecular bands arising from the atmosphere of a relatively cold M-dwarf companion. At these wavelengths, the presence of the Ca triplet in emission reveals a temperature inversion in the atmosphere of the companion owing to the heating of its atmosphere. This heating is thought to be caused by the interaction of the magnetic field with the atmosphere of the M-dwarf (e.g. Geng et al. 2016; Katz 2017; Garnavich et al. 2019). In addition to the narrow emission components, in SDSSJ2306 we can identify (at least in some of the strongest lines), a broad- low-amplitude secondary emission component seen at least in Hα, similar to AR Sco and J1912. As can be seen in Fig. 5, the strength of the emission lines in SDSSJ2306 is also modulated with the orbital period. As discussed above, the same is true for the pulse fraction of the signal producing P_{ω}, exhibiting a minimum roughly when the trailing face of the companion star is facing away from Earth. This may be related to the partial occultation of the high excitation region site likely located on the trailing face of the companion. A similar effect has been reported in AR Sco by Garnavich et al. (2019); these authors show how this region produces the bulk of He II λ4686 Å in the WD pulsar prototype.

In general, the pulsed emission on WD pulsars is thought to arise predominately from synchrotron radiation, which dominates across the electromagnetic spectrum. Since there is virtually no accretion in these systems, the X-ray emission is also dominated by the pulsed emission, at least in AR Sco and J1912. Unfortunately, we do not have any pointed X-ray observations of SDSSJ2306 and it is not detected by the *ROSAT* all-sky survey (Voges et al. 1999). However, we can use the upper limit of ≈ 0.004 ct/s from *ROSAT* to obtain an upper limit of $L_X < 2 \times 10^{-31} (d/1.2\,{\rm kpc})^2$ erg/s in the 0.1 – 2.4 keV band assuming a simple power law with photon index of 2 and adopting the extinction to hydrogen column density conversion from Güver & Özel (2009). This upper limit lies in the lower band of X-ray luminosities observed accreting WDs suggesting the actual luminosity for SDSSJ2306 is lower than the typical CV (e.g. Pretorius & Knigge 2012; Pretorius & Mukai 2014; Schwope 2018). Combining this with the average SDSS g-band magnitude ($g \approx 21$ mag) we obtain $\log(L_X/L_{\rm opt}) < 0.21$, in line with other WD pulsars. On the

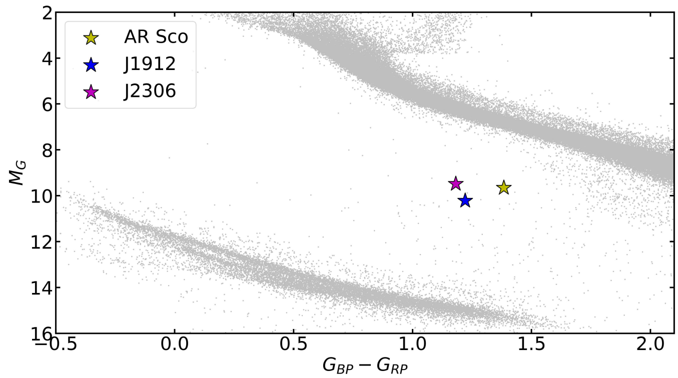

Figure 10. Gaia colour-magnitude diagram. AR Sco, J1912 and SDSSJ2306 are indicated with green, blue and pink stars respectively. All three systems are in a similar region of the parameter space between the WD sequence and the main sequence (bottom and top grey clusters, respectively).

other end of the electromagnetic spectrum, preliminary results from Sahu et al. (in prep) show a detection of SDSSJ2306 with the Karl G. Jansky Very Large Array telescope (VLA) at 6 cm (Band C), however, further analysis is required to determine the presence of pulsed emission similar to the one seen in other WD pulsars (Stanway et al. 2018; Pelisoli et al. 2023).

Another of the common characteristics of WD pulsars is the strong linear polarization observed at optical wavelengths. AR Sco is the most extreme case, exhibiting up to 40 per cent linear polarization (Buckley et al. 2017). In J1912 the polarized emission is more modest, with up to 12 per cent of linear polarization, but with a pulse morphology and orbital phasing very similar to AR Sco (Potter & Buckley 2018; Pelisoli et al. 2023). There are no photopolarimetric observations of SDSSJ2306, however, it is an excellent candidate given how similar this new WD pulsar is to AR Sco. Finally, as we show in Fig. 10, despite the small number of identified systems in the sample, the position of WD pulsars on the HR diagram seems to be clustered around absolute magnitudes $M_G \simeq 10$ mag in the *Gaia* *G*-band and $G_{\rm BP} - G_{\rm RP} \simeq 1.25$ (see Sec. 3.4 for a discussion on the distance), a relatively unexplored region of the *Gaia* colour-magnitude diagram (e.g. Abrahams et al. 2022; Pelisoli et al. 2025). This suggests that the (time averaged) spectral components dominating at these wavelengths may be produced by the same physical process. The low number of WD pulsar discovered, combined with their clustering in the parameter spaces discussed in this section, suggests that the formation of WD pulsars requires fairly constrained stellar and orbital properties in their progenitor systems. This interpretation aligns with previous theoretical studies by Schreiber et al. (2021).

In summary, the observational properties of SDSSJ2306 presented in this research (i.e. spin and orbital periods, pulse morphology, companion star) reveal this new system as a sibling of AR Sco and the third system of the class.

4.2 Evolutionary pathways

The evolution of WD pulsars is an interesting open topic, in particular in connection with long period radio transients (LPTs). The origin of LPTs is uncertain, but two were found to be binary systems harbouring a WD with an M-dwarf companion (Hurley-Walker et al. 2024; de Ruiter et al. 2025) which exhibit relatively bright radio pulses with a frequency consistent with the orbital period (de Ruiter et al. 2025; Rodriguez 2025). Given the observational properties of this new class of radio transients, in particular the lack of a detected WD spin period, they have been postulated as an intermediate evolutionary configuration between WD pulsars and strongly magnetized CVs, i.e. polars, where the WD spin has synchronised with the orbit. The low temperatures observed in the WDs in LPTs ($5-7\times10^3$ K) require the hypothetical progenitors (WD pulsars) to not have had any accretion-induced heating episode in the past; in fact, their temperature must have been already relatively low during the WD pulsar stage (c.f. Townsley & Bildsten 2004; Althaus et al. 2010). However, the observed WD temperature of the closest known WD pulsars ($T_{\rm WD} \simeq 11500$ K; Garnavich et al. 2021; Pelisoli et al. 2024) challenges this hypothesis. In contrast, this high temperature is consistent with WD pulsars having undergone an accretion-driven heating (and consequent spin up) episode in the past. This is consistent with the evolutionary model of Schreiber et al. (2021) and also with the pulsed emission mechanism proposed by Lyutikov et al. (2020), which additionally requires the WD to have a low magnetic field, in agreement with recent observational constrains of AR Sco's WD (Barrett & Gurwell 2025).

A potential evolutionary connection has also been drawn with magnetic propellers, which are proposed to share the same emission model as WD pulsars in Lyutikov et al. (2020). At a first glance this in agreement with the parameter space occupied by these two types of systems (see Sec. 4.1). However, there is a fundamental difference between them; AE Aqr is thought to have gone through a thermal timescale mass transfer (TTSMT, Paczynski et al. 1969) as a consequence of a relatively massive donor at the time at which the system came into contact. This TTSMT, in turn, spun up the WD to match the present-day high spin periods (c.f. Schenker & King 2002). During this process, the companion star loses a significant part of its envelope, changing its external composition. The footprint of such a process can be detected in the strength of the ultraviolet spectral lines. As shown in Castro Segura et al. (2023), the extreme line ratios seen in some accreting binaries (e.g. Mauche et al. 1997; Haswell et al. 2002; Schenker et al. 2002; Gänsicke et al. 2003) can only be explained by the CNO-equilibrium abundances of a (previously) relatively massive companion star, suggesting that the companion stars have lost their hydrogen envelope. While ultraviolet spectroscopy of AE Aqr matches this scenario, the same cannot be said about the two WD pulsars observed in the UV (Garnavich et al. 2021; Pelisoli et al. 2024), suggesting that WD pulsars and magnetic propellers have indeed followed a different formation channel.

5 CONCLUSION

We presented the discovery of a new WD pulsar, SDSS J230641.47+244055.8. We have used long-term photometric data from ZTF to determine a precise orbital period of $P_{\rm orb} = 3.4939558(3)$ h. Fast photometry obtained with ULTRASPEC was used to determine the spin period $P_{\rm spin} = 92$ s. Folding the light curve onto the spin period reveals a double pulsed emission profile with major and minor peaks similar to the that observed in AR Sco. The orbital ephemeris was obtained through time-resolved spectroscopy and we used the amplitude from the radial velocity solutions to determine the mass function of the system. SDSSJ2306's stellar companion was constrained to be a M4.0 ± 0.5 M-dwarf with an effective temperature $T_{\rm eff} \approx 3300$ K. By subtracting the non-stellar emission we estimated the normalization factor (R_2/d). We estimated the distance to the system to be about 1.2 kpc, which in turn, constrains the companion to be in the mass range $0.19\,{\rm M}_\odot \lesssim M_2 \lesssim 0.28\,{\rm M}_\odot$ for Roche lobe filling factors

≥ 0.8. All these properties reveal this new object to be a sibling of AR Sco and the third system of the class of WD pulsars.

We have compiled a comprehensive table of the observational properties exhibited by all three known WD pulsars, establishing a benchmark that will inform the classification of future discoveries within this rare class of objects. We discussed the proposed evolutionary scenarios for WD pulsars. We ruled out a potential evolutionary connection with the recently discovered long-period radio transients (LPTs) hosting white dwarfs, due to the significantly higher temperatures observed in WD pulsars ($T_{\rm WD} \simeq 11500$ K) compared to those in LPTs (5000–7000 K). This temperature difference implies cooling timescales that are too long to support a direct evolutionary link. Finally, we considered the possibility that the progenitor evolutionary channel of WD pulsars is the same as that of magnetic propellers (i.e., AE Aqr-like systems). If this were the case, WD pulsars would have been spun up during a thermal-timescale mass transfer (TTMT) phase, during which the system would be detectable as a super-soft X-ray source. Such an episode would remove most of the companion's envelope, thus exposing its core. However, there is no observational evidence of such a scenario in known WD pulsars. Therefore, we can rule out the possibility that WD pulsars were spun up via a TTMT phase. At the time of writing, the only theory that successfully explains the observed configuration of WD pulsars is the model proposed by Schreiber et al. (2021), which requires the white dwarf to have been magnetized prior to the onset of accretion (e.g., Isern et al. 2017). However, the origin of the magnetic field in WD pulsars remains a mystery.

ACKNOWLEDGEMENTS

We dedicate this work to the memory of Prof. Tom Marsh, whose contributions to the development of ULTRASPEC and characterisation of AR Sco, the first known white dwarf pulsar, have left a lasting legacy in the field.

NCS and DLC acknowledge support from the Science and Technology Facilities Council (STFC) grant ST/X001121/1. IP acknowledges support from the Royal Society through a University Research Fellowship (URF\R1\231496). DS acknowledges support from the Science and Technology Facilities Council (STFC), grant numbers ST/T007184/1, ST/T003103/1, ST/T000406/1, ST/X001121/1 and ST/Z000165/1. This project has received funding from the European Research Council (ERC) under the European Union's Horizon 2020 research and innovation programme (Grant agreement No. 101020057). AA acknowledges support from Naresuan University (NU), and National Science Research and Innovation Fund (NSRF), grant no. R2568B019.

This work has made use of data obtained at the Thai National Observatory on Doi Inthanon, operated by NARIT.

This research made use of Astropy, a community-developed core Python package for Astronomy (Astropy Collaboration et al. 2018). Based on observations obtained at the international Gemini Observatory, a program of NSF NOIRLab, which is managed by the Association of Universities for Research in Astronomy (AURA) under a cooperative agreement with the U.S. National Science Foundation on behalf of the Gemini Observatory partnership: the U.S. National Science Foundation (United States), National Research Council (Canada), Agencia Nacional de Investigación y Desarrollo (Chile), Ministerio de Ciencia, Tecnología e Innovación (Argentina), Ministério da Ciência, Tecnologia, Inovações e Comunicações (Brazil), and Korea Astronomy and Space Science Institute (Republic of Korea).

ZTF is supported by the National Science Foundation under Grants No. AST-1440341 and AST-2034437 and a collaboration including current partners Caltech, IPAC, the Oskar Klein Center at Stockholm University, the University of Maryland, University of California, Berkeley , the University of Wisconsin at Milwaukee, University of Warwick, Ruhr University, Cornell University, Northwestern University and Drexel University. Operations are conducted by COO, IPAC, and UW.

Funding for the Sloan Digital Sky Survey V has been provided by the Alfred P. Sloan Foundation, the Heising-Simons Foundation, the National Science Foundation, and the Participating Institutions. SDSS acknowledges support and resources from the Center for High-Performance Computing at the University of Utah. SDSS telescopes are located at Apache Point Observatory, funded by the Astrophysical Research Consortium and operated by New Mexico State University, and at Las Campanas Observatory, operated by the Carnegie Institution for Science. The SDSS web site is `www.sdss.org`.

SDSS is managed by the Astrophysical Research Consortium for the Participating Institutions of the SDSS Collaboration, including Caltech, The Carnegie Institution for Science, Chilean National Time Allocation Committee (CNTAC) ratified researchers, The Flatiron Institute, the Gotham Participation Group, Harvard University, Heidelberg University, The Johns Hopkins University, L'Ecole polytechnique fédérale de Lausanne (EPFL), Leibniz-Institut für Astrophysik Potsdam (AIP), Max-Planck-Institut für Astronomie (MPIA Heidelberg), Max-Planck-Institut für Extraterrestrische Physik (MPE), Nanjing University, National Astronomical Observatories of China (NAOC), New Mexico State University, The Ohio State University, Pennsylvania State University, Smithsonian Astrophysical Observatory, Space Telescope Science Institute (STScI), the Stellar Astrophysics Participation Group, Universidad Nacional Autónoma de México, University of Arizona, University of Colorado Boulder, University of Illinois at Urbana-Champaign, University of Toronto, University of Utah, University of Virginia, Yale University, and Yunnan University.

AFFILIATIONS

[1] *Department of Physics, University of Warwick, Gibbet Hill Road, Coventry, CV4 7AL, UK*
[2] *Department of Physics, Faculty of Science, Naresuan University, Phitsanulok 65000, Thailand*
[3] *Universidade Federal do Rio Grande do Sul (UFRGS), Departamento de Astronomia - IF Av. Bento Gonçalves, 9500 Campus do Vale 91540-000 - Porto Alegre - RS, Brazil*
[4] *Astrophysics Research Cluster, School of Mathematical and Physical Sciences, University of Sheffield, Sheffield, S3 7RH, United Kingdom*
[5] *Instituto de Astrofísica de Canarias, E-38205 La Laguna, Tenerife, Spain*
[6] *School of Physics, University College Cork, Cork, T12 K8AF, Ireland*
[6] *School of Physics, University College Cork, Cork, T12 K8AF, Ireland*
[7] *Homer L. Dodge Department of Physics and Astronomy, University of Oklahoma, 440 W. Brooks Street, Norman, OK 73019, USA*
[8] *JILA, University of Colorado and National Institute of Standards and Technology, 440 UCB, Boulder, CO 80309-0440, USA*
[9] *Hamburger Sternwarte, University of Hamburg, Gojenbergsweg 112, 21029 Hamburg, Germany*
[10] *South African Astronomical Observatory, P.O Box 9, Observatory,*

7935 Cape Town, South Africa
[11]*Department of Astronomy, University of Cape Town, Private Bag X3, Rondebosch 7701, South Africa*

DATA AVAILABILITY

The data underlying this article is publicly available in the corresponding telescope archives: *Sloan Digital Sky Survey* `https://www.sdss.org`, *Zwicky Transient Facility* `https://www.ztf.caltech.edu` and *Gemini* `https://archive.gemini.edu` Remaining data will be shared on reasonable request to the corresponding author.

REFERENCES

Abrahams E. S., Bloom J. S., Szkody P., Rix H.-W., Mowlavi N., 2022, ApJ, 938, 46
Allard F., Hauschildt P. H., Alexander D. R., Starrfield S., 1997, ARA&A, 35, 137
Althaus L. G., Córsico A. H., Isern J., García-Berro E., 2010, A&ARv, 18, 471
Astropy Collaboration et al., 2018, AJ, 156, 123
Aungwerojwit A., Gänsicke B. T., Rodríguez-Gil P., Hagen H. J., Giannakis O., Papadimitriou C., Allende Prieto C., Engels D., 2007, A&A, 469, 297
Bagnulo S., Landstreet J. D., 2022, ApJ, 935, L12
Bailer-Jones C. A. L., Rybizki J., Fouesneau M., Demleitner M., Andrae R., 2021, AJ, 161, 147
Barrett P. E., Gurwell M. A., 2025, arXiv e-prints, p. arXiv:2505.06468
Bellm E. C., et al., 2019a, PASP, 131, 018002
Bellm E. C., et al., 2019b, PASP, 131, 068003
Beniamini P., Hotokezaka K., van der Horst A., Kouveliotou C., 2019, MNRAS, 487, 1426
Blanton M. R., et al., 2017, AJ, 154, 28
Brinkworth C. S., Marsh T. R., Dhillon V. S., Knigge C., 2006, MNRAS, 365, 287
Brown A. J., et al., 2022, MNRAS, 513, 3050
Buckley D. A. H., Meintjes P. J., Potter S. B., Marsh T. R., Gänsicke B. T., 2017, Nature Astronomy, 1, 0029
Camisassa M., Fuentes J. R., Schreiber M. R., Rebassa-Mansergas A., Torres S., Raddi R., Dominguez I., 2024, A&A, 691, L21
Castro Segura N., et al., 2023, MNRAS,
Castro-Tapia M., Zhang S., Cumming A., 2024, ApJ, 975, 63
Chen X., Wang S., Deng L., de Grijs R., Yang M., Tian H., 2020, ApJS, 249, 18
Dekany R., et al., 2020, PASP, 132, 038001
Dhillon V. S., et al., 2014, MNRAS, 444, 4009
Dhillon V. S., et al., 2021, MNRAS, 507, 350
Eggleton P. P., 1983, ApJ, 268, 368
Fitzpatrick E. L., 1999, PASP, 111, 63
Foreman-Mackey D., Hogg D. W., Lang D., Goodman J., 2013, PASP, 125, 306
Friend M. T., Martin J. S., Smith R. C., Jones D. H. P., 1990, MNRAS, 246, 654
Gaia Collaboration et al., 2023, A&A, 674, A1
Gänsicke B. T., et al., 2003, ApJ, 594, 443
Gänsicke B. T., Araujo-Betancor S., Hagen H. J., Harlaftis E. T., Kitsionas S., Dreizler S., Engels D., 2004, A&A, 418, 265
Garnavich P., Littlefield C., Kafka S., Kennedy M., Callanan P., Balsara D. S., Lyutikov M., 2019, ApJ, 872, 67
Garnavich P., Littlefield C., Lyutikov M., Barkov M., 2021, ApJ, 908, 195
Geng J.-J., Zhang B., Huang Y.-F., 2016, ApJ, 831, L10
Graham M. J., et al., 2019, PASP, 131, 078001
Green G. M., Schlafly E., Zucker C., Speagle J. S., Finkbeiner D., 2019, ApJ, 887, 93
Güver T., Özel F., 2009, MNRAS, 400, 2050
Haefner R., Fiedler A., Butler K., Barwig H., 2004, A&A, 428, 181
Hardy L. K., et al., 2017, MNRAS, 465, 4968
Haswell C. A., Hynes R. I., King A. R., Schenker K., 2002, MNRAS, 332, 928
Hook I. M., Jørgensen I., Allington-Smith J. R., Davies R. L., Metcalfe N., Murowinski R. G., Crampton D., 2004, PASP, 116, 425
Hurley-Walker N., et al., 2024, ApJ, 976, L21
Inight K., et al., 2023, MNRAS, 524, 4867
Isern J., García-Berro E., Külebi B., Lorén-Aguilar P., 2017, ApJ, 836, L28
Ivezić Ž., Connolly A. J., VanderPlas J. T., Gray A., 2014, Statistics, Data Mining, and Machine Learning in Astronomy: A Practical Python Guide for the Analysis of Survey Data, doi:10.1515/9781400848911.
Joshi A., 2025, AJ, 169, 269
Katz J. I., 2017, ApJ, 835, 150
Knigge C., Baraffe I., Patterson J., 2011, ApJS, 194, 28
Lomb N. R., 1976, Ap&SS, 39, 447
Lyutikov M., Barkov M., Route M., Balsara D., Garnavich P., Littlefield C., 2020, arXiv e-prints, p. arXiv:2004.11474
Marsh T. R., et al., 2016, Nature, 537, 374
Mauche C. W., Lee Y. P., Kallman T. R., 1997, ApJ, 477, 832
Muñoz-Darias T., Casares J., Martínez-Pais I. G., 2005, ApJ, 635, 502
Mukai K., 2017, PASP, 129, 062001
Nelder J. A., Mead R., 1965, The Computer Journal, 7, 308
Paczynski B., Ziólkowski J., Zytkow A., 1969, in Hack M., ed., Astrophysics and Space Science Library Vol. 13, Mass Loss from Stars. p. 237, doi:10.1007/978-94-010-3405-0_30
Pala A. F., et al., 2017, MNRAS, 466, 2855
Pala A. F., et al., 2020, MNRAS, 494, 3799
Parsons S. G., Marsh T. R., Copperwheat C. M., Dhillon V. S., Littlefair S. P., Gänsicke B. T., Hickman R., 2010, MNRAS, 402, 2591
Parsons S. G., et al., 2018, MNRAS, 481, 1083
Pelisoli I., et al., 2022a, MNRAS, 509, L31
Pelisoli I., et al., 2022b, MNRAS, 516, 5052
Pelisoli I., et al., 2023, Nature Astronomy, 7, 931
Pelisoli I., et al., 2024, MNRAS, 527, 3826
Pelisoli I., et al., 2025, MNRAS,
Potter S. B., Buckley D. A. H., 2018, MNRAS, 481, 2384
Pretorius M. L., Knigge C., 2012, MNRAS, 419, 1442
Pretorius M. L., Mukai K., 2014, MNRAS, 442, 2580
Rea N., et al., 2024, ApJ, 961, 214
Rodriguez A. C., 2025, A&A, 695, L8
Rodriguez A. C., et al., 2025, PASP, 137, 014201
Savage B. D., Mathis J. S., 1979, ARA&A, 17, 73
Scargle J. D., 1982, ApJ, 263, 835
Scaringi S., et al., 2015, Science Advances, 1, e1500686
Schaffenroth V., Barlow B. N., Pelisoli I., Geier S., Kupfer T., 2023, A&A, 673, A90
Schenker K., King A. R., 2002, in Gänsicke B. T., Beuermann K., Reinsch K., eds, Astronomical Society of the Pacific Conference Series Vol. 261, The Physics of Cataclysmic Variables and Related Objects. p. 242 (`arXiv:astro-ph/0110187`)
Schenker K., King A. R., Kolb U., Wynn G. A., Zhang Z., 2002, MNRAS, 337, 1105
Schlafly E. F., Finkbeiner D. P., 2011, ApJ, 737, 103
Schreiber M. R., Belloni D., Gänsicke B. T., Parsons S. G., Zorotovic M., 2021, Nature Astronomy, 5, 648
Schwope A. D., 2018, A&A, 619, A62
Schwope A., Marsh T. R., Standke A., Pelisoli I., Potter S., Buckley D., Munday J., Dhillon V., 2023, A&A, 674, L9
Stanway E. R., Marsh T. R., Chote P., Gänsicke B. T., Steeghs D., Wheatley P. J., 2018, A&A, 611, A66
Takata J., Hu C. P., Lin L. C. C., Tam P. H. T., Pal P. S., Hui C. Y., Kong A. K. H., Cheng K. S., 2018, ApJ, 853, 106
Townsley D. M., Bildsten L., 2004, ApJ, 600, 390
VanderPlas J. T., 2018, ApJS, 236, 16
VanderPlas J. T., Ivezić Ž., 2015, ApJ, 812, 18
Voges W., et al., 1999, A&A, 349, 389
Voikhanskaya N. F., 1987, Soviet Astronomy Letters, 13, 250

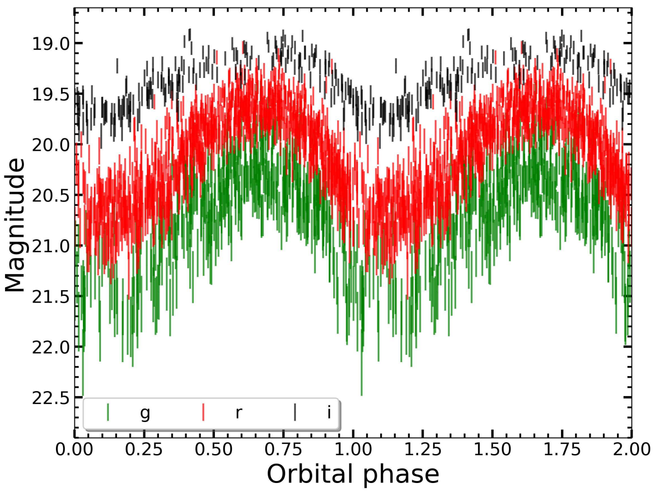

Figure A1. Light curves from ZTF folded into the orbital period.

Warner B., 1995, Cataclysmic variable stars. Vol. 28

Wright M. H., 1996, in Griffiths D. F., Watson G. A., eds, Numerical Analysis 1995: Proceedings of the 1995 Dundee Biennial Conference in Numerical Analysis. Addison Wesley Longman, Harlow, UK, pp 191–208

Zorotovic M., Schreiber M. R., Gänsicke B. T., 2011, A&A, 536, A42

de Ruiter I., et al., 2025, Nature Astronomy,

du Plessis L., Venter C., Wadiasingh Z., Harding A. K., Buckley D. A. H., Potter S. B., Meintjes P. J., 2022, MNRAS, 510, 2998

APPENDIX A: LONG-TERM PHOTOMETRIC LIGHT CURVES

Photometric light curves from ZTF folded into the orbital period obtained from multi-band Lomb-Scargle analysis are shown in Fig. A1. The orbital phase was obtained from spectroscopic measurements presented in 3.2.